

# A Collisional Model Approach to Quantum Phase Sensitivity

S. Elham Mousavigharalari<sup>1</sup> and Deniz Türkpençe<sup>1, 2, \*</sup>

<sup>1</sup>*İstanbul Technical University, Informatics Institute, 34469 Maslak, İstanbul, Turkey*

<sup>2</sup>*Qready Quantum Technologies, ITU ARI Teknokent, 34467 İstanbul, Turkey*

(Dated: September 23, 2025)

We investigate how relative phase information, encoded by a single qubit  $H\varphi H$  gate sequence, is reflected in the quantum Fisher information (QFI) under noisy dynamics. Within a collision model framework, algorithmically prepared reservoir units imprint a  $\varphi$  dependent signature on the steady state of a probe qubit, which permits a closed form evaluation of the QFI. To corroborate this reservoir based prediction, we perform a device level simulation of the same gate sequence using effective two level dynamics with parameters motivated by transmon devices. In this description the noisy gate segment is modeled by a Gaussian modulated drive evolving under open system dynamics. Across both treatments the resulting QFI profile exhibits the same qualitative dependence on the encoded phase, despite the distinct underlying mechanisms. Beyond conceptual agreement, the steady state perspective provides a tomography free metric for phase fragility that can inform biased noise error correction and guide compiler and pulse choices in near term quantum hardware.

## I. INTRODUCTION

Today's quantum computers operate in the Noisy Intermediate-Scale Quantum (NISQ) era [1]. As a result, intensive efforts are underway, both in hardware and at the algorithmic level, to develop methods that allow quantum error correction (QEC) algorithms to function below their error threshold [2–7]. Quantum supremacy, which would enable the effective execution of algorithms like Shor's [8] and HHL [9], is anticipated to emerge with large-scale, fault-tolerant qubit systems—in other words, through the efficient implementation of error correction techniques. Because these algorithms encode critical information in relative phases, and because phase-flip errors are dominant in some noisy quantum hardware, this information becomes more fragile [10, 11].

This reality makes new approaches to quantifying the fragility of phase information under noisy hardware conditions highly relevant [12, 13]. Quantum Fisher Information is a crucial mathematical tool in quantum metrology for estimating the precision of a quantum state's parameters [14, 15]. However, calculating QFI requires knowledge of the state's density matrix ( $\rho$ ), which in turn necessitates complex measurements like quantum state tomography (QST) across different basis. Even for a single basis measurement, a high number of experimental repetitions are needed to statistically average the outcomes. This process is complex, involving statistical effects such as shot noise inherent to measurement. These challenges motivate the development of approaches that assess phase-sensitive properties of quantum states directly from their noisy pre-measurement description.

The quantum collision model [16–22] has become a frequently employed method for describing open quantum systems, primarily due to the flexibility it offers in characterizing the degrees of freedom of the environment. A

standard collision model [16–19] emulates a dissipative and Markovian open quantum system dynamic through repeated, sequential interactions between identical reservoir units and a designated quantum probe. This process, also referred to as quantum homogenization [17, 18], culminates in the probe system reaching a stable or 'steady state', which can be either a state of thermal equilibrium or a non-equilibrium state [20, 21]. In this steady state, certain properties of the reservoir are encoded dissipatively onto the probe system.

The reservoir units can be prepared in a mixed state to represent a thermal reservoir at a finite temperature [23], or they can be prepared in a pure state as characterized by parameters on the Bloch sphere. This type of model is also consistent with the concept of a 'quantum information reservoir' [24–27] found in the literature.

This study is based on the premise that a noisy quantum computer's pre-measurement state can be modeled as a noisy quantum reservoir. Within this framework, a *collision model* is employed to investigate the interaction between a quantum probe qubit and an information reservoir composed of algorithmically prepared noisy units. The primary objective is to investigate the estimation of parameters embedded within the steady state attained by the probe qubit.

According to the analytical solution derived from the *master equation*, which we developed to describe the open quantum system dynamics of the collision model [26, 27], the probe qubit's steady state consistently carries information with a measurable precision dependent on a specific parameter value. To prepare the reservoir qubits, a gate sequence of  $H\varphi H$  was used, consisting of a *Hadamard gate* ( $H$ ) and a *phase-shift gate* ( $\varphi$ ).

This gate sequence serves as a device-independent, algorithmic representation of the *Mach-Zehnder interferometer* [28–31], a common tool in quantum metrology experiments. The fact that device-level simulations, performed with the same algorithm and parameters, yield a similar Quantum Fisher Information ( $F_\varphi$ ) function for the pre-measurement density matrix, provides a crucial

\* [dturkpence@itu.edu.tr](mailto:dturkpence@itu.edu.tr)

verification. This result suggests that a collision-model-based noisy quantum reservoir approach is a suitable method for parameter estimation in noisy quantum computing hardware.

This manuscript is organized as follows. Section II introduces the collision–model framework and formulates the probe–reservoir dynamics leading to the steady–state density matrix, along with an analysis of mutual information as a preliminary diagnostic. Section III derives the analytical expression of the probe’s quantum Fisher information by inserting the steady–state solution into the Bloch–vector form of QFI. Section IV presents the device–level simulation of the  $H\varphi H$  gate sequence under Gaussian–modulated drives and open–system dynamics, allowing a direct comparison with the collision–model predictions. Section V discusses the implications of these findings for quantum error correction, compiler–level optimization, and hardware–aware algorithm design, and outlines possible generalizations to multi–qubit probes and correlated reservoirs. Finally, Section VI summarizes the main conclusions and highlights avenues for future work.

## II. PRELIMINARIES

The quantum collision model, also known as the repeated interaction model, provides a fundamental framework for simulating the dynamics of an open quantum system. In its simplest form, this model describes a probe system undergoing a sequence of identical interactions with individual, freshly prepared reservoir units. This repetitive process drives the probe system towards a steady state over a finite period [32, 33].

The dynamics of a single collision step can be precisely characterized by a quantum dynamical map, which is inherently completely positive and trace-preserving (CPTP). This map, denoted here as  $\Lambda$ , transforms the system’s state according to the following expression:

$$\Lambda[\rho_S] = \text{Tr}_{\mathcal{R}}[U_{S\mathcal{R}}(\rho_S \otimes \rho_{\mathcal{R}})U_{S\mathcal{R}}^\dagger] \quad (1)$$

Here,  $\rho_S$  represents the quantum state of the system of interest, and  $\rho_{\mathcal{R}}$  is the initial state of a reservoir unit, which is typically prepared in a thermal or pure state.  $U_{S\mathcal{R}}$  is the unitary operator describing the brief interaction between the system and the reservoir unit. The trace operation,  $\text{Tr}_{\mathcal{R}}$ , effectively averages over the degrees of freedom of the reservoir, yielding the updated state of the system.

When the reservoir is conceptualized as an information reservoir, it can be useful to examine the quantum mutual information between the probe system and the reservoir units. The mutual information that quantifies how much information has flowed from the reservoir unit to the probe is

$$\mathcal{I}(S : R_i) = S\left(\rho_S^{(i)}\right) + S\left(\rho_{R_i}\right) - S\left(\rho_{S\mathcal{R}_i}^{(i)}\right) \quad (2)$$

where  $S(\rho) = -\text{Tr}[\rho \log_2 \rho]$  is the von Neumann entropy. Here,  $\rho_{S\mathcal{R}_i}^{(i)}$  is the joint density matrix immediately after the  $i$ -th collision,  $\rho_S^{(i)} = \text{Tr}_{R_i} \rho_{S\mathcal{R}_i}^{(i)}$  is the updated probe state and  $\rho_{R_i} = \text{Tr}_S \rho_{S\mathcal{R}_i}^{(i)}$  is the outgoing ancilla state that is subsequently traced out.

The sensitivity of parameter estimation in both classical and quantum regimes is quantified by Fisher information. For a classical system described by a parameterized probability distribution  $\{p_r(\lambda)\}$  over a set of discrete outcomes  $r$ , the classical Fisher information is given by:

$$\mathcal{F}_\lambda = \sum_r p_r(\lambda) \left[ \frac{\partial \ln p_r(\lambda)}{\partial \lambda} \right]^2 \quad (3)$$

In quantum mechanics, this concept is generalized to the quantum Fisher information (QFI),  $\mathcal{F}_\lambda$ . QFI is defined via the symmetric logarithmic derivative (SLD),  $L_\lambda$ , which is implicitly given by the equation  $\partial_\lambda \rho_\lambda = \frac{1}{2}\{\rho_\lambda, L_\lambda\}$  [34]. This leads to the fundamental expressions for QFI:

$$\begin{aligned} \mathcal{F}_\lambda = & \sum_i \frac{(\partial_\lambda p_i)^2}{p_i} + \sum_i p_i \mathcal{F}_{\lambda,i} \\ & - \sum_{i \neq j} \frac{8p_i p_j}{p_i + p_j} |\langle \psi_i | \partial_\lambda \psi_j \rangle|^2. \end{aligned} \quad (4)$$

For a general mixed quantum state with the spectral decomposition  $\rho_\lambda = \sum_i p_i(\lambda) |\psi_i\rangle\langle\psi_i|$ , the QFI can be explicitly calculated from the evolution of its eigenvalues and eigenvectors. The full formula is composed of two terms: one related to the change in eigenvalues and another capturing the evolution of the eigenstates themselves, as shown below:

$$\begin{aligned} \mathcal{F}_\lambda = & \sum_i \frac{[\partial_\lambda p_i(\lambda)]^2}{p_i(\lambda)} \\ & + \sum_{i \neq j} \frac{2(p_i(\lambda) - p_j(\lambda))^2}{p_i(\lambda) + p_j(\lambda)} |\langle \psi_i | \partial_\lambda \psi_j \rangle|^2. \end{aligned} \quad (5)$$

The operational significance of Fisher information is established by the Cramér–Rao bound, which states that the variance of any unbiased estimator  $\hat{\lambda}$  of a parameter  $\lambda$  is constrained as

$$\text{Var}(\hat{\lambda}) \geq \frac{1}{M \mathcal{F}_\lambda}, \quad (6)$$

where  $M$  denotes the number of independent measurement repetitions. In the quantum setting, replacing the classical Fisher information with the QFI yields the quantum Cramér–Rao inequality, which sets the ultimate precision limit permitted by quantum mechanics [34, 35]. Thus, QFI directly quantifies the best possible sensitivity to changes in a parameter, independent of the specific measurement strategy.

An alternative, and particularly useful, form of the Fisher formula exists for two-level systems (TLS), which

are prevalent in quantum information. This compact expression, elegantly links the QFI to the derivatives of the density matrix as [36, 37]

$$\mathcal{F}_\lambda = \text{Tr}[(\partial_\lambda \rho)^2] + \frac{1}{\det \rho_\lambda} \text{Tr}[(\rho_\lambda \partial_\lambda \rho_\lambda)^2]. \quad (7)$$

For TLS, it is often convenient to express the density matrix in Bloch-vector form,  $\rho = \frac{1}{2}(\mathbb{I} + \mathbf{r} \cdot \boldsymbol{\sigma})$ , where  $|\mathbf{r}| \leq 1$  and  $\boldsymbol{\sigma}$  is the vector of Pauli matrices. In this representation, the QFI can be written as

$$\mathcal{F}_\lambda = |\partial_\lambda \mathbf{r}|^2 + \frac{(\mathbf{r} \cdot \partial_\lambda \mathbf{r})^2}{1 - |\mathbf{r}|^2}, \quad (8)$$

which is particularly suitable for mixed states with  $|\mathbf{r}| < 1$ . For pure states ( $|\mathbf{r}| = 1$ ), the formula reduces to  $\mathcal{F}_\lambda = |\partial_\lambda \mathbf{r}|^2$  by taking the appropriate limit [37].

The sensitivity of our parameter estimation relies entirely on the final, steady-state density matrix  $\rho_\lambda$  of the probe system, which is achieved after its repeated interaction within the information reservoir. The primary objective of this work, as noted previously, is to analyze the QFI of a probe quantum system that reaches a steady state under the influence of noisy, algorithmically parameterized quantum information reservoirs in a collision model. This analysis will be benchmarked against the QFI calculated from an equivalent noisy quantum algorithm on a single-qubit quantum computer. Specifically, this comparison will be performed by computing the QFI from two distinct sources: the steady-state density matrix of the probe system in the collision model and the density matrix obtained from a device-level simulation of the noisy  $H\varphi H$  sequence.

The dynamics of the device-level simulation will be evaluated within the open system framework [38]. The evolution of the density operator is governed by a time-dependent Lindblad equation of the form

$$\begin{aligned} \frac{d}{dt} \rho(t) = & -\frac{i}{\hbar} [H(t), \rho(t)] \\ & + \sum_k \gamma_k \left( L_k \rho(t) L_k^\dagger - \frac{1}{2} \{ L_k^\dagger L_k, \rho(t) \} \right), \end{aligned} \quad (9)$$

where  $H(t)$  denotes the system Hamiltonian under an external drive, while the dissipative channels are captured by the Lindblad operators  $L_k$  with associated rates  $\gamma_k$ . Formally, the solution can be written in terms of a time-ordered exponential of the Liouvillian superoperator,

$$\rho(t) = \mathcal{T} \exp \left( \int_0^t \mathcal{L}(t') dt' \right) \rho(0), \quad (10)$$

where  $\mathcal{L}(t)$  acts on the density matrix. This expression highlights the non-trivial role of time ordering when the Hamiltonian is explicitly time dependent, as is often the case in quantum control methods [39, 40].

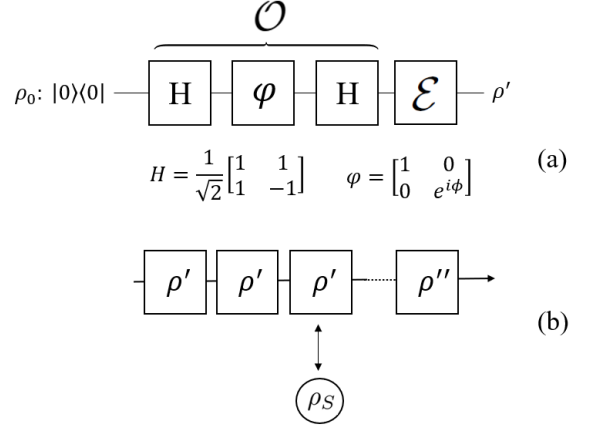


FIG. 1. Schematic of the proposed protocol. (a) Reservoir-qubit preparation: each unit is initialized to  $\rho_0$ , then evolves under the unitary sequence  $H\varphi H$ , and finally undergoes a phenomenological noise channel  $\mathcal{E}$ , yielding the mixed state  $\rho'$ . (b) Collision dynamics: reservoir units in state  $\rho'$  are injected one by one into the probe channel, interacting sequentially with the probe qubit  $\rho_S$ , and imprinting their phase-dependent information on its steady state.

### III. MODEL AND SYSTEM DYNAMICS

The fragility of valuable quantum information under realistic noisy conditions has motivated researchers to better understand the behavior of information under decoherence and dissipation not merely as a source loss, but as a novel computational resource [41]. Our work centers on a paradigm that quantum reservoirs need not merely function as irreversible sinks for system information, but can instead act as structured communication channels, transferring specific signatures of the environment to the system [21, 42, 43].

In this context, the quantum collision model offers a powerful framework for analytically tracking how parameter-dependent features of an engineered quantum information reservoir become imprinted on the steady state of a probe system. Its tractability enables the derivation of master equations that allow direct evaluation of Quantum Fisher Information (QFI) under realistic noise conditions.

Fig. 1 provides an overview of the proposed framework, illustrating (a) the noisy initialization of individual reservoir units and (b) their sequential interactions with a probe system within a collision model. In this scheme, both the reservoir units and the probe system are modeled as two-level quantum systems (qubits).

The information-reservoir qubits are prepared by first applying the single-qubit gate sequence  $\mathcal{O} = H\varphi H$  with  $H$  the Hadamard gate and  $\varphi$  a relative-phase rotation—and subsequently subjecting the output to a phenomenological noise channel  $\mathcal{E}$ . The net noisy preparation map is therefore  $\tilde{\mathcal{O}} = \mathcal{E} \circ \mathcal{O}$ , which acts on the initial state  $\rho_0$  to produce the identical, non-interacting reser-

ervoir state  $\rho' = \tilde{\mathcal{O}}[\rho_0] = \mathcal{E}(\mathcal{O}\rho_0\mathcal{O}^\dagger)$ .

In this study, the information reservoir is explicitly defined as a collection of  $n$  uncorrelated, identical qubit states, collectively represented by the tensor product:

$$\rho_{\mathcal{R}} = \bigotimes_{i=1}^n \rho'_i(\phi). \quad (11)$$

The overall quantum dynamical map for a sequence of  $n$  collisions, taking place over a total time of  $n\tau$ , can be expressed as a nested composition of trace operations, which describes the sequential interaction of the probe system with each reservoir unit:

$$\Lambda_{n\tau}[\rho_S] = \text{Tr}_n[U_n \dots \text{Tr}_1[U_1(\rho_S \otimes \rho'_1)U_1^\dagger] \otimes \dots \otimes \rho'_n U_n^\dagger]. \quad (12)$$

Here,  $\tau$  represents the duration of a single collision, and  $U_i = e^{-i\mathcal{H}_i\tau}$  is the unitary propagator for the  $i$ -th interaction step. The total Hamiltonian for this interaction is given by  $\mathcal{H}_i = \mathcal{H}_{S,i}^{\text{free}} + \mathcal{H}_{S,i}^{\text{int}}$ , where the free term and the interaction term are defined as:

$$\mathcal{H}_{S,i}^{\text{free}} = \frac{\hbar\omega_S}{2}\sigma_S^z + \frac{\hbar\omega_i}{2}\sigma_i^z, \quad (13)$$

$$\mathcal{H}_{S,i}^{\text{int}} = \hbar g(\sigma_S^+ \sigma_i^- + \text{h.c.}). \quad (14)$$

In these expressions,  $\sigma_S^z$  and  $\sigma_i^z$  are the Pauli- $z$  operators for the probe system and the  $i$ -th reservoir unit, respectively, with corresponding frequencies  $\omega_S$  and  $\omega_i$ . In general, we take  $\omega_S = \omega_i$  for each collision step. The operators  $\sigma^+$  and  $\sigma^-$  denote the standard raising and lowering operators, and  $g$  is the coupling constant characterizing the strength of the partial-swap interaction.

### 1. Collisional Mutual Information

Understanding the sensitivity of parametric information transferred from a quantum information reservoir first necessitates a foundational analysis of the mutual information dynamics. Specifically, an investigation into the  $\phi$ -dependent evolution of mutual information between the probe qubit and the reservoir units, within the collision model framework, can provide a crucial basis for subsequent analysis.

Fig. 2 shows the mutual information between the probe qubit and the phase-parameterized information reservoir. The quantum state of each noisy reservoir unit, which is prepared by applying phenomenological noise to the algorithmic protocol in Fig. 1(a), can be straightforwardly shown to be:

$$\rho' = \begin{bmatrix} \frac{1+\cos\phi}{2}e^{-t/T_1} & \frac{i\sin\phi}{2}e^{-t/T_2} \\ -\frac{i\sin\phi}{2}e^{-t/T_2} & \frac{1-\cos\phi}{2}e^{-t/T_1} \end{bmatrix}. \quad (15)$$

Numerical simulations were performed with the QUTIP library [44], adopting the convention  $\hbar = 1$  throughout. For the dissipation and dephasing times in

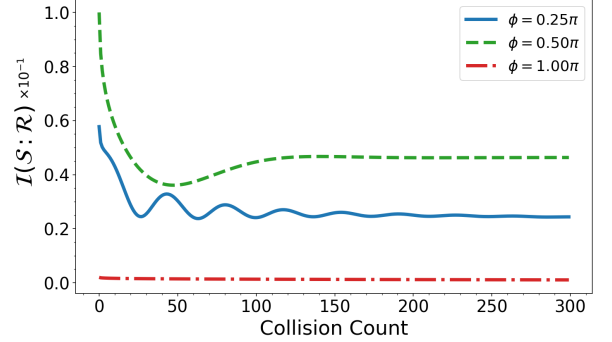


FIG. 2. Mutual information between probe qubit and reservoir units based on different values of  $\phi$  against the collision count. The noisy preparation of each reservoir ancilla uses phenomenological relaxation times  $T_1 = 150 \mu\text{s}$  and  $T_2 = 100 \mu\text{s}$ , entering through exponential factors. The level splittings for the probe and reservoir qubits are,  $\omega_S = \omega_R \equiv 1$ . The probe-ancilla coupling rate  $g = 0.1$  and collision duration  $\tau = 0.12$  are dimensionless and in units of  $1/\omega_S$ .

Eq. (15), we chose characteristic superconducting-qubit relaxation parameters,  $T_1$  and  $T_2$ , on the order of  $\mu\text{s}$ . The noise-exposure interval of each reservoir ancilla was set to  $t = 480 \text{ ns}$ , which corresponds to the execution time of roughly three single-qubit logic gates in current hardware [45]. The probe is initialized in the superposition state  $|+\rangle = (|0\rangle + |1\rangle)/\sqrt{2}$  in order to maximally sense the phase information that the reservoir imprints during the dissipative, repeated-interaction dynamics. As shown in Fig. 2, the mutual information  $\mathcal{I}(S:\mathcal{R})$  generated between the probe and the reservoir depends strongly on the reservoir phase  $\phi$  and relaxes to distinct steady values for the three choices of  $\phi$ . The smallest steady value occurs for  $\phi = \pi$ , whereas the largest is observed for  $\phi = \frac{\pi}{2}$ .

In the noisy preparation  $\rho'(\phi)$  the transverse coherence and population imbalance scale as  $|\rho'_{01}| = \frac{1}{2}e^{-t/T_2}|\sin\phi|$  and  $e^{-t/T_1}\cos\phi$ , respectively. Because the exchange-type interaction generates correlations through the coherent  $\{|01\rangle, |10\rangle\}$  manifold, the steady mutual information follows this coherence envelope: it is largest near  $\phi = \frac{\pi}{2}$ , where the reservoir has equal populations and maximal  $|\rho'_{01}|$ , and it is smallest near  $\phi = \pi$  (and  $\phi \approx 0$ ), where  $\rho'_{01} \approx 0$  and the state is effectively  $\sigma_z$ -eigenlike and therefore weakly coupled for correlation build-up. The observed  $\phi$ -selective behavior is thus a direct consequence of how dephasing ( $T_2$ ) limits accessible coherence and how the interaction converts that coherence into system-reservoir correlations.

### 2. Micromaser Master Equation

Micromaser systems [46, 47], long a cornerstone for elucidating light-matter interactions, provide an experimental platform; we therefore adopt them as a paradigmatic model for deriving master equations for repeated

interactions [48, 49].

To connect the stroboscopic collision picture with a continuous-time description, we follow the standard micromaser coarse-graining for a *single* information reservoir composed of identically prepared ancillae. After every encounter the ancilla is discarded and reset to the fixed state  $\rho'(\phi)$ . Each collision of duration  $\tau$  is generated, in the interaction picture, by the partial-swap Hamiltonian given in Eq. (14), so that the step propagator is  $U_i(\tau) = \exp[-i H_{\text{int}}^{(i)} \tau / \hbar]$ . Expanding to second order in  $\tau$ ,

$$U_i(\tau) \simeq 1 - i\tau V - \frac{\tau^2}{2} V^2, \quad (16)$$

$$V \equiv \frac{1}{\hbar} H_{\text{int}}^i = g(\sigma_S^+ \sigma_i^- + \sigma_S^- \sigma_i^+). \quad (17)$$

Collisions arrive according to a Poisson process with rate  $r$ . During a short interval  $\delta t$ , with probability  $r \delta t$  a collision takes place; otherwise the state remains unchanged. Writing the pre-collision joint state as  $\rho_S(t) \otimes \rho'$ , the coarse-grained probe update reads [27]

$$\begin{aligned} \rho_S(t + \delta t) &= (1 - r \delta t) \rho_S(t) \\ &+ r \delta t \text{Tr}_{\mathcal{R}} [U(\tau) \rho_S(t) \otimes \rho' U^\dagger(\tau)]. \end{aligned} \quad (18)$$

Subtracting  $\rho_S(t)$ , dividing by  $\delta t$ , and taking the limit  $\delta t \rightarrow 0$  yields

$$\dot{\rho}_S(t) = r \text{Tr}_{\mathcal{R}} [U(\tau) \rho_S(t) \otimes \rho' U^\dagger(\tau) - \rho_S(t) \otimes \rho']. \quad (19)$$

Keeping terms up to  $\mathcal{O}(\tau^2)$  in the propagator expansion and tracing out the ancilla, the dynamics take the Lindblad form (See Appendix A)

$$\begin{aligned} \dot{\rho}_S(t) &= -i [H_{\text{eff}}, \rho_S(t)] + \Gamma_+ \mathcal{L}[\sigma_S^+](\rho_S(t)) \\ &+ \Gamma_- \mathcal{L}[\sigma_S^-](\rho_S(t)), \end{aligned} \quad (20)$$

where the effective Hamiltonian and dissipative rates are

$$H_{\text{eff}} = r \tau \hbar g (\langle \sigma^- \rangle_{\rho'} \sigma_S^+ + \langle \sigma^+ \rangle_{\rho'} \sigma_S^-), \quad (21)$$

$$\Gamma_+ = \frac{r \tau^2 g^2}{2} \langle \sigma^+ \sigma^- \rangle_{\rho'}, \quad \Gamma_- = \frac{r \tau^2 g^2}{2} \langle \sigma^- \sigma^+ \rangle_{\rho'}. \quad (22)$$

Here, the notation  $\langle O \rangle_{\rho'} \equiv \text{Tr}[O \rho']$  denotes expectation values over the prepared ancilla state, and the Lindblad superoperator is defined as  $\mathcal{L}[o](\rho) \equiv 2 o \rho o^\dagger - o^\dagger o \rho - \rho o^\dagger o$ . Equation (20) is a CP-divisible generator that captures how the engineered reservoir imprints its phase-dependent fingerprint on the probe through random, repeated interactions.

Having obtained the master equation, we now proceed to determine the steady-state density matrix of the probe qubit by setting  $\dot{\rho}_S(t) = 0$  in the master equation. For a single information reservoir, the steady-state density matrix takes the form

$$\begin{aligned} \rho_S^{\text{ss}} &= \langle \sigma^+ \sigma^- \rangle_{\rho'} |0\rangle\langle 0| + \langle \sigma^- \sigma^+ \rangle_{\rho'} |1\rangle\langle 1| \\ &+ [i \gamma^- (\langle \sigma^+ \sigma^- \rangle_{\rho'} - \langle \sigma^- \sigma^+ \rangle_{\rho'}) |0\rangle\langle 1| + \text{H.c.}], \end{aligned} \quad (23)$$

where  $\gamma^- = r \tau g \langle \sigma^- \rangle_{\rho'}$ . Here, the expectation values  $\langle O \rangle_{\rho'}$  are taken with respect to the prepared ancilla state.

## IV. ANALYTICAL AND NUMERICAL ANALYSIS

In this section, we present a comparative study between the analytical expressions derived from the steady-state solution of the micromaser master equation and the numerical evaluation of quantum Fisher information (QFI) obtained from device-level noisy quantum simulations. The analytical results highlight how phase sensitivity is encoded in the asymptotic density matrix, while the numerical analysis employs circuit-level noise models to capture hardware-specific imperfections. By aligning these approaches, we aim to establish a consistent framework that links theoretical predictions with realistic experimental scenarios.

### 1. Quantum Fisher Information

The central objective of this study is to demonstrate that, within a collision model framework, coherently encoded parametric information from an algorithmically prepared and noisy quantum information reservoir can be transferred to a probe system in the steady state. Furthermore, we show that this parametric imprint serves as an indicator of parametric sensitivity in a noisy quantum computer undergoing the same algorithmic process.

In this context, by substituting the matrix elements from Eq. (15) into Eq. (23), the steady-state of the probe qubit, is obtained as (See Appendix B)

$$\rho_S^{\text{ss}} = \begin{bmatrix} \frac{1+\cos\phi}{2} e^{-\gamma_1 t} & \frac{\zeta}{2} \sin\phi \cos\phi e^{-(\gamma_1+\gamma_2)t} \\ \frac{\zeta}{2} \sin\phi \cos\phi e^{-(\gamma_1+\gamma_2)t} & \frac{1-\cos\phi}{2} e^{-\gamma_1 t} \end{bmatrix}, \quad (24)$$

where,  $\gamma_1 \equiv 1/T_1$ ,  $\gamma_2 \equiv 1/T_2$  and  $\zeta \equiv r \tau g$ .

Although the steady state remains mixed, the persistence of finite off-diagonal elements indicates that quantum phase correlations survive through steady coherence [50, 51]. Such enduring coherence becomes especially relevant for dissipative quantum computing, where environmental coupling can be engineered as a functional resource rather than being treated solely as a detrimental effect.

Thus, by simply substituting the steady-state density matrix obtained above into Eq. (8), the sensitivity of the probe qubit to the parametric information transferred from the quantum information reservoir can be evaluated in terms of the QFI as (See Appendix C)

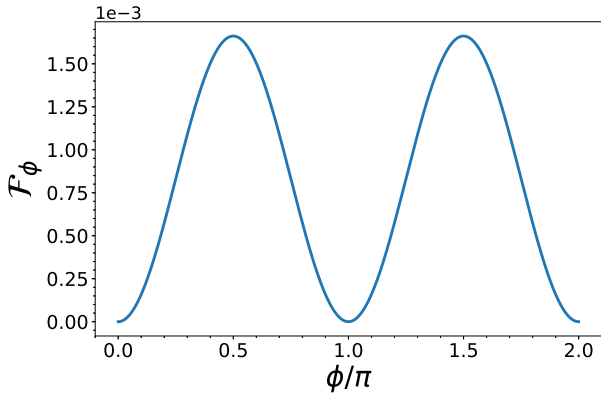


FIG. 3. Quantum Fisher information  $\mathcal{F}_\phi$  of the probe qubit as a function of the encoded phase  $\phi$ . The noisy dynamics are modeled with phenomenological relaxation times  $T_1 = 150 \mu\text{s}$  and  $T_2 = 100 \mu\text{s}$ , incorporated through exponential damping factors. The probe and reservoir qubits are assumed to have equal level splittings,  $\omega_S = \omega_R \equiv 1$ . The probe–ancilla interaction is characterized by a dimensionless coupling strength  $g = 0.1$  and a collision duration  $\tau = 0.12$ , both expressed in units of  $1/\omega_S$ .

$$\begin{aligned} \mathcal{F}_\phi = & \zeta^2 e^{-2(\gamma_1+\gamma_2)t} \cos^2(2\phi) + e^{-2\gamma_1 t} \sin^2 \phi \\ & + \frac{1}{4} \sin^2(2\phi) \left[ \zeta^2 e^{-2(\gamma_1+\gamma_2)t} \cos(2\phi) - e^{-2\gamma_1 t} \right]^2 \\ & \frac{1}{1 - e^{-2\gamma_1 t} \cos^2 \phi - \frac{\zeta^2}{4} e^{-2(\gamma_1+\gamma_2)t} \sin^2(2\phi)} \end{aligned} \quad (25)$$

The steady state quantum Fisher information (QFI) obtained in Fig. 3 exhibits a distinct dependence on the parameter  $\phi$ . The functional form shows maxima around  $\phi = \pi/2$  and  $3\pi/2$ , whereas values close to  $\phi = \pi$  yield a pronounced minimum. This behavior arises from the competing roles of the longitudinal component  $r_z(\phi) = e^{-\gamma_1 t} \cos \phi$  and the transverse component  $r_x(\phi) = \frac{\zeta}{2} e^{-(\gamma_1+\gamma_2)t} \sin(2\phi)$  of the Bloch vector. When  $\phi$  is tuned to  $\pi/2$ , the population imbalance disappears, and the probe qubit is driven towards the equatorial plane. In this regime, even small variations of  $\phi$  induce significant changes in the state, which explains the enhanced sensitivity. Conversely, around  $\phi = \pi$  the probe state aligns nearly along the  $z$  direction, where exponential damping suppresses the accessible coherence, resulting in minimal QFI.

The resulting sensitivity therefore directly reflects how efficiently parametric information can be encoded into the probe through the reservoir induced dynamics. In particular, the exponential suppression governed by the characteristic times  $T_1$  and  $T_2$  determines the effective lifetime of this sensitivity. In the analytic expression,  $\zeta = gr\tau$  fixes the interaction scale and the ancilla noise-exposure time  $t$  determines the exponential damping; together they set the amplitude of the oscillatory terms

appearing in the numerator of the QFI.

When compared with the mutual information dynamics, a parallel trend is observed. The mutual information between the probe and the ancillae grows with the number of collisions and reaches a plateau that depends on  $\phi$ . Larger values are obtained for  $\phi = \pi/2$ , while  $\phi = \pi$  produces the lowest steady correlations. Although QFI and mutual information quantify different aspects — one being a local estimator of parameter sensitivity and the other capturing total correlations — both are governed by the reservoir coherence profile. This correspondence confirms that maximal sensitivity and maximal system–reservoir correlations emerge at the same operating points of  $\phi$ .

## 2. Device-level simulation

In contrast to the collision-based reservoir framework, this section addresses a direct device-level approach where the  $H\varphi H$  sequence is modeled as a driven evolution of a phenomenological two-level transmon qubit approximation under Gaussian-modulated control pulses [52, 53]. The simulation employs realistic circuit parameters and decoherence constants in order to generate the pre-measurement density matrix. The resulting state is then used in the Fisher information expression, where derivatives with respect to the encoded parameter are obtained numerically through finite element method evaluation. This framework enables a structural comparison with the collision model by highlighting how sensitivity emerges from hardware-level dynamics rather than from sequential reservoir interactions.

We begin by considering the implementation of the Hadamard gate in a form consistent with the native compilation adopted in current IBMQ devices [45]. In this framework the operation is decomposed as  $H = R_z[\frac{\pi}{2}] R_x[\frac{\pi}{2}] R_z[\frac{\pi}{2}]$ . Since both  $R_z$  rotations and the intermediate parameter shift  $\varphi$  can be realized as virtual frame updates [45], they do not introduce additional noise. Consequently, the only physically driven operation in this sequence is the  $R_x[\pi/2]$  rotation, which is implemented as a single-qubit microwave pulse. In order to reflect realistic control conditions, we model this drive by a Gaussian-modulated envelope.

Within this description the qubit is treated as an effective two-level transmon, driven by a classical oscillatory electric field. The dynamics are described by the Hamiltonian

$$H(t) = \frac{\hbar\omega_0}{2} \sigma_z + \Omega(t) \cos(\omega_D t) \sigma_x, \quad (26)$$

where  $\omega_0$  is the transition frequency of the qubit,  $\omega_D$  denotes the drive frequency, and  $\Omega(t)$  is the time-dependent Rabi frequency. This choice captures the essential features of experimental single-qubit control without invoking further corrections such as higher-level leakage [54], which are beyond the present scope. The modulation is

chosen as

$$\Omega(t) = \Omega_0 \exp\left(-\frac{(t - t_c)^2}{\sigma_p^2}\right), \quad (27)$$

with  $\Omega_0$  the peak amplitude,  $t_c$  the temporal center of the pulse, and  $\sigma_p$  the width of the Gaussian envelope. The amplitude parameter  $\Omega_0$  specifies the maximum Rabi frequency reached during the Gaussian pulse and is given by  $\Omega_0 = \frac{\alpha}{\sqrt{\pi} \sigma_p}$ , with the derivation provided in Appendix D. Here,  $\alpha = \int_{-\infty}^{\infty} \Omega(t) dt$  denotes the dimensionless pulse area, which directly corresponds to the rotation angle of the Bloch vector, thereby quantifying the net qubit rotation induced by the drive.

In the device-level model, virtual  $z$ -axis phase updates  $R_z[\alpha]$  are treated as ideal frame rotations, whereas the  $x$ -axis quarter-turns  $R_x[\frac{\pi}{2}]$  are realized by a Gaussian-modulated drive and therefore evolve under the open-system dynamics in Eqs. (9)–(10). We define the noiseless phase-update channel as  $\mathcal{U}_z[\beta](\rho) = R_z[\beta] \rho R_z^\dagger[\beta]$  where  $\beta$  denotes the applied phase shift, and the noisy  $x$ -rotation channel as

$$\mathcal{E}_x[\frac{\pi}{2}](\rho) = \mathcal{T} \exp\left(\int_0^{T_x} \mathcal{L}(t) dt\right) \rho, \quad (28)$$

with  $\mathcal{L}(t)$  the time-dependent Liouvillian generated by the control Hamiltonian  $H(t)$  and the jump operators  $L_1 = \sigma_-$  and  $L_\phi = \sigma_z$  at rates  $\Gamma_1 = 1/T_1$  and  $\gamma_\phi = 1/T_2 - 1/(2T_1)$ .

The complete channel implementing the noisy  $H\varphi H$  sequence is then

$$\Phi_{\text{dev}}(\varphi) = \mathcal{U}_z[\frac{\pi}{2}] \circ \mathcal{E}_x[\frac{\pi}{2}] \circ \mathcal{U}_z[\varphi + \pi] \circ \mathcal{E}_x[\frac{\pi}{2}] \circ \mathcal{U}_z[\frac{\pi}{2}], \quad (29)$$

so that the output state is  $\rho_{\text{out}} = \Phi_{\text{dev}}(\varphi)[\rho_0]$ . Note that  $\mathcal{U}_z[\varphi + \pi]$  is equivalent to the phase gate  $\varphi = \text{diag}(1, e^{i\phi})$  up to an unobservable global phase. To enable a parameter-matched comparison with the collision-model analysis, we use the same dissipation constants as in Fig. 2, namely  $T_1 = 150 \mu\text{s}$  and  $T_2 = 100 \mu\text{s}$ .

The numerical derivative of  $\rho(\varphi)$  entering Eq. (7) was obtained via a finite-difference scheme (See Appendix D). The resulting evaluation of the device-level model yields the QFI curve shown in Fig. 4. Despite the fact that the dynamics here are governed by a driven open-system Hamiltonian and Lindblad operators, rather than the collision process considered previously, the  $\phi$ -dependence of the QFI exhibits similar qualitative features as the analytical prediction from the reservoir model. In particular, maxima appear near  $\phi = \pi/2$  and  $3\pi/2$ , while a relative minimum is observed at  $\phi = \pi$ , where the sensitivity is reduced but remains finite. This alignment demonstrates that the steady state analysis of the collision framework and the time-resolved simulation of a noisy hardware primitive converge to consistent conclusions regarding parameter sensitivity, even though the underlying mechanisms are fundamentally different.

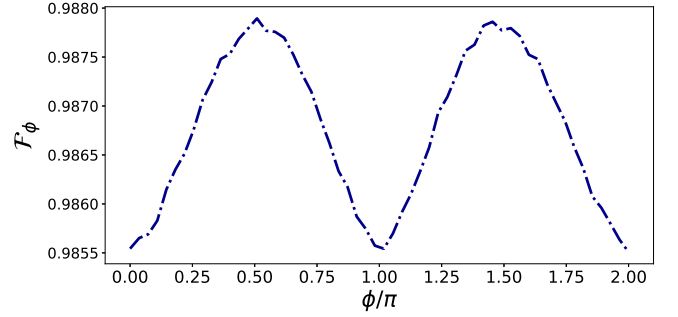


FIG. 4. Quantum Fisher Information  $\mathcal{F}_\phi$  obtained from the device-level simulation of the noisy  $H\varphi H$  sequence. The simulation employs an effective two-level qubit with transition frequency  $\omega_0 = 2\pi \times 4.5 \text{ GHz}$ , driven by a Gaussian-modulated  $x$ -pulse of width  $\sigma_p = 22.4 \text{ ns}$  and normalized pulse area  $\alpha = \pi/2$ . Dissipative channels are included through  $T_1 = 150 \mu\text{s}$  and  $T_2 = 100 \mu\text{s}$ , identical to those used in the reservoir-based model.

While the Cramér–Rao inequality sets the ultimate lower bound on the variance of any unbiased estimator in terms of the quantum Fisher information  $\mathcal{F}_\phi$ , and the Standard Quantum Limit (SQL) is typically invoked to describe a  $1/\sqrt{M}$  scaling with the number of independent trials  $M$ , our analysis extracts  $\mathcal{F}_\phi$  directly from the steady-state density operator of the probe. In this way, the attainable phase-estimation accuracy is quantified in an open-system scenario without resorting to projective measurement statistics. By evaluating  $\mathcal{F}_\phi$  solely from  $\rho^{\text{ss}}(\phi)$ , we capture the entire phase sensitivity available before readout, thereby identifying the degree of phase fragility that noisy gate constructions inherently possess. This perspective underlines that a reservoir engineered steady state can already encode the essential metrological information, offering a resource-efficient means to benchmark phase response without full tomographic reconstruction.

Placed alongside the device-level simulation, which computes  $F_\phi$  from a noisy  $H\varphi H$  sequence under Lindblad dynamics, the collision-model predictions and hardware-motivated numerics exhibit parallel qualitative features (see Fig. 4). Both approaches highlight enhanced sensitivity near  $\varphi = \pi/2$  and  $3\pi/2$ , as well as a reduced, though finite, response at  $\varphi = \pi$ . This alignment demonstrates that two very different dynamical descriptions — repeated interactions with a noisy reservoir and a pulse-resolved hardware model — converge to consistent statements about achievable parameter sensitivity.

## V. IMPLICATIONS AND OUTLOOK

A key outcome of this work is a practical, tomography-free method for predicting the phase-sensitivity profile  $\mathcal{F}_\varphi$  of a quantum device’s pre-measurement state. Such a capability has direct implications for the efficient

implementation of quantum error–correction (QEC) protocols on NISQ hardware [5, 7, 55, 56]. QEC relies on syndrome measurements [55, 57], which are metrological procedures for inferring error syndromes with the highest precision allowed by quantum mechanics. Knowledge of the functional dependence  $\mathcal{F}_\varphi$  enables tailoring of syndrome extraction strategies to the phase regime where the system is most sensitive, thereby improving the likelihood of correctly identifying phase–flip errors and maximizing the effectiveness of the chosen error correction code.

This is particularly valuable for deploying biased noise QEC codes, which achieve higher fault tolerance thresholds when phase errors dominate [58]. By mapping  $\mathcal{F}_\varphi$  across qubits, one can identify operating points and devices where such codes offer the greatest benefit, allowing hardware–aware allocation of QEC resources. For example, regions with high  $\mathcal{F}_\varphi$  indicate heightened sensitivity to phase errors, suggesting the use of phase robust stabilizer configurations or realigned measurement bases, while low  $\mathcal{F}_\varphi$  regions correspond to “sweet spots” where operations are naturally more resilient to phase fluctuations and coherent detuning errors [12, 13].

Beyond QEC, the knowledge of  $\mathcal{F}_\varphi$  can guide compiler and pulse level optimizations [52, 53, 59]. The  $\mathcal{F}_\varphi$  profile serves as a phase sensitivity blueprint for compilation stacks, enabling decomposition of unitaries into native gate sequences that avoid highly phase sensitive angles. This reduces the accumulation of coherent phase errors and mitigates  $T_2$  limited dephasing without additional overhead. Likewise, optimal control pulse parameters (e.g., DRAG shaping [40, 54, 60]) can be tuned to steer the qubit dynamics toward regions of lower phase sensitivity, improving the overall circuit fidelity. Moreover, for multi qubit architectures, constructing a spatial map of  $\mathcal{F}_\varphi$  across the device can guide compilation strategies. It allows the most phase sensitive algorithmic layers, such as the entangling stages in variational quantum algorithms, to be placed on the qubits that exhibit the greatest phase robustness, while less sensitive operations can be assigned to qubits that are more prone to noise. Such hardware–aware allocation is expected to maximize the fidelity of large scale compiled circuits.

A further motivation for employing the collision model description is its unique ability to yield analytical and scalable insight that complements direct device level simulations. Whereas a full time domain simulation must be repeated numerically for every parameter setting, the collision framework produces closed form steady state solutions that allow rapid parameter sweeps and transparent identification of the roles played by  $T_1$ ,  $T_2$ , and interaction strength  $g$ . This analytical tractability turns the model into a lightweight “theoretical laboratory” where one can systematically vary noise channels, introduce non–Markovian effects, or embed correlations among ancillae without the computational overhead of full master–equation numerics. The modular structure of the approach also makes it naturally extensible to many–qubit

reservoirs and composite environments, enabling scalable exploration of how collective dissipation or entanglement within the bath modifies the imprint left on the probe. By benchmarking the collision model predictions against pulse level simulations, as done here, one not only validates the simplified description but also gains a fast, interpretable tool that can guide the design of noise aware protocols and reservoir engineered schemes for future quantum devices.

Although this study focused on a single–qubit probe, the methodology is not restricted to this case. Composite collision models [19] naturally generalize to multi–qubit reservoirs, permitting investigation of how correlations and entanglement within the environment influence the probe’s steady state. On the probe side, one may employ entangled registers as sensors to explore metrological enhancements such as Heisenberg limited scaling of QFI. Even with a single probe, sequential interaction with correlated ancilla clusters could probe how reservoir correlations affect information transfer. Exploring these directions will clarify whether the agreement between collision model predictions and device level simulations persists in larger Hilbert spaces and could inspire reservoir engineering strategies optimized for phase sensitive parameter estimation in many qubit architectures.

## VI. CONCLUSIONS

This work presented a dual perspective on the sensitivity of relative phase information in noisy quantum devices. By deriving closed form analytical expressions within a collision–model framework and validating them against device level simulations based on Gaussian driven two–level dynamics, we established that the quantum Fisher information  $\mathcal{F}_\varphi$  carries a consistent phase dependent signature across two fundamentally different descriptions. This agreement underscores that the steady state of a probe qubit can faithfully encode metrological information about an algorithmically prepared reservoir, even in the presence of dissipation and dephasing.

Beyond providing theoretical insight, the approach developed here offers a practical, tomography–free route to quantify phase fragility in near term quantum hardware. The resulting  $\mathcal{F}_\varphi$  profile acts as a direct indicator of phase sensitivity, guiding the placement of error correction resources, stabilizer design, and compiler level gate synthesis toward regimes where phase errors are either most detectable or least detrimental. In this way, the method links open system theory with actionable metrics for hardware–aware quantum algorithm deployment.

Finally, the analytical tractability of the collision model makes it a versatile platform for exploring more complex scenarios, including correlated reservoirs, non–Markovian noise, and entangled probes. Future investigations could extend this framework to multi–qubit settings, providing a scalable path toward understanding how environmental correlations influence parameter

estimation in large scale processors and informing the design of reservoir engineered protocols for next generation quantum technologies.

## ACKNOWLEDGMENTS

This work was supported by the Scientific and Technological Research Council of Turkey (TÜBİTAK, Grant No. 124F472). We also acknowledge the facilities and technical support provided by the Informatics Institute of İstanbul Technical University and the Qready Quantum Technologies and Consulting Joint Stock Company.

## Appendix A: Unitary expansion and the master equation

We set  $\hbar = 1$ . In each collision the joint state factorizes as  $\rho(t) = \rho_S(t) \otimes \rho'$ , where the ancilla is reset to the prepared state  $\rho'$  after tracing. The interaction-picture propagator for a collision of duration  $\tau$  is

$$U(\tau) = e^{-iH_{\text{int}}\tau}. \quad (\text{A1})$$

We expand the propagator to second order in  $\tau$ ,

$$U(\tau) \simeq \mathbb{1} - V_1(\tau) - V_2(\tau), \quad (\text{A2})$$

$$V_1(\tau) = i\tau H_{\text{int}}, \quad (\text{A3})$$

$$V_2(\tau) = \frac{\tau^2}{2} H_{\text{int}}^2, \quad (\text{A4})$$

which can be written using the Lindblad superoperator  $\mathcal{L}[o]\rho = 2opo^\dagger - o^\dagger o\rho - \rho o^\dagger o$ , where the anti-commutator is defined as  $\{A, B\} \equiv AB + BA$ .

Collecting all terms, the micromaser-type master equation for a single reservoir is

$$\begin{aligned} \dot{\rho}_S(t) = & -i[H_{\text{eff}}, \rho_S(t)] + \Gamma_+ \mathcal{L}[\sigma_S^+]\rho_S(t) \\ & + \Gamma_- \mathcal{L}[\sigma_S^-]\rho_S(t), \end{aligned} \quad (\text{A12})$$

with rates

$$\begin{aligned} \Gamma_+ &= \frac{1}{2} r g^2 \tau^2 \langle \sigma_S^- \sigma_S^+ \rangle_{\rho'}, \\ \Gamma_- &= \frac{1}{2} r g^2 \tau^2 \langle \sigma_S^+ \sigma_S^- \rangle_{\rho'}. \end{aligned} \quad (\text{A13})$$

Here  $\langle O \rangle_{\rho'} = \text{Tr}(O \rho')$  denotes the expectation value over the prepared ancilla.

with the single-ancilla interaction Hamiltonian  $H_{\text{int}}$ . For randomly injected ancillas at rate  $r$  (Poisson process), the short-time update of the reduced system state reads

$$\begin{aligned} \rho_S(t + \delta t) = & (1 - r \delta t) \rho_S(t) \\ & + r \delta t \text{Tr}_R(U(\tau) [\rho_S(t) \otimes \rho'] U^\dagger(\tau)), \end{aligned} \quad (\text{A5})$$

which, in the limit  $\delta t \rightarrow 0$ , leads to the master equation

$$\dot{\rho}_S(t) = r \text{Tr}_R(U(\tau) [\rho_S(t) \otimes \rho'] U^\dagger(\tau) - \rho_S(t) \otimes \rho'). \quad (\text{A6})$$

Inserting the second-order expansion and discarding  $O(\tau^3)$  terms,

$$U\rho U^\dagger \simeq \rho - V_1\rho - \rho V_1^\dagger - V_2\rho - \rho V_2^\dagger + V_1\rho V_1^\dagger, \quad (\text{A7})$$

so that

$$\dot{\rho}_S(t) = r \text{Tr}_R \left( -V_1\rho - \rho V_1^\dagger - V_2\rho - \rho V_2^\dagger + V_1\rho V_1^\dagger \right). \quad (\text{A8})$$

The first-order contribution gives a coherent term,

$$-V_1\rho - \rho V_1^\dagger = -i\tau [H_{\text{int}}, \rho] \Rightarrow \text{Tr}_R(\cdot) = -i\tau [H_{\text{eff}}, \rho_S], \quad (\text{A9})$$

with the effective drive

$$H_{\text{eff}} = r g \tau (\langle \sigma_S^- \rangle_{\rho'} \sigma_S^+ + \langle \sigma_S^+ \rangle_{\rho'} \sigma_S^-). \quad (\text{A10})$$

The second-order contribution produces dissipation. After tracing out the ancilla one obtains

$$\begin{aligned} V_1\rho V_1^\dagger - \frac{1}{2} \{H_{\text{int}}^2, \rho\} = & \frac{\tau^2}{2} g^2 \left( 2\langle \sigma_S^- \sigma_S^+ \rangle_{\rho'} \sigma_S^+ \rho_S \sigma_S^- - \langle \sigma_S^- \sigma_S^+ \rangle_{\rho'} \{ \sigma_S^- \sigma_S^+, \rho_S \} \right. \\ & \left. + 2\langle \sigma_S^+ \sigma_S^- \rangle_{\rho'} \sigma_S^- \rho_S \sigma_S^+ - \langle \sigma_S^+ \sigma_S^- \rangle_{\rho'} \{ \sigma_S^+ \sigma_S^-, \rho_S \} \right), \end{aligned} \quad (\text{A11})$$

## Appendix B: Steady state density matrix

Starting from Eq. (23), we insert the ancilla expectation values of Eq. (15) and use

$$\gamma^- \equiv r \tau g \langle \sigma^- \rangle_{\rho'} = \zeta \langle \sigma^- \rangle_{\rho'}, \quad (\text{B1})$$

$$\zeta \equiv r \tau g, \gamma_1 \equiv \frac{1}{T_1}, \gamma_2 \equiv \frac{1}{T_2}. \quad (\text{B2})$$

From Eq. (15) one finds

$$\langle \sigma^+ \sigma^- \rangle_{\rho'} = \frac{1+\cos\phi}{2} e^{-\gamma_1 t}, \quad (\text{B3})$$

$$\langle \sigma^- \sigma^+ \rangle_{\rho'} = \frac{1-\cos\phi}{2} e^{-\gamma_1 t}, \quad (\text{B4})$$

$$\langle \sigma^- \rangle_{\rho'} = -\frac{i}{2} \sin\phi e^{-\gamma_2 t}. \quad (\text{B5})$$

Substituting the first two lines into Eq. (23) gives

$$\begin{aligned} \rho_S^{\text{ss}} &= \begin{bmatrix} \frac{1+\cos\phi}{2} e^{-\gamma_1 t} & i\gamma^- \left( \frac{1+\cos\phi}{2} - \frac{1-\cos\phi}{2} \right) e^{-\gamma_1 t} \\ \text{H.c.} & \frac{1-\cos\phi}{2} e^{-\gamma_1 t} \end{bmatrix} \\ &= \begin{bmatrix} \frac{1+\cos\phi}{2} e^{-\gamma_1 t} & i\gamma^- \cos\phi e^{-\gamma_1 t} \\ -i(\gamma^-)^* \cos\phi e^{-\gamma_1 t} & \frac{1-\cos\phi}{2} e^{-\gamma_1 t} \end{bmatrix}. \end{aligned} \quad (\text{B6})$$

Using  $\gamma^- = \zeta \langle \sigma^- \rangle_{\rho'} = \zeta \left( -\frac{i}{2} \sin\phi e^{-\gamma_2 t} \right)$  and its conjugate, the off-diagonal entries become

$$i\gamma^- \cos\phi e^{-\gamma_1 t} = \frac{\zeta}{2} \sin\phi \cos\phi e^{-(\gamma_1+\gamma_2)t},$$

so that the steady state takes the compact form

$$\rho_S^{\text{ss}} = \begin{bmatrix} \frac{1+\cos\phi}{2} e^{-\gamma_1 t} & \frac{\zeta}{2} \sin\phi \cos\phi e^{-(\gamma_1+\gamma_2)t} \\ \frac{\zeta}{2} \sin\phi \cos\phi e^{-(\gamma_1+\gamma_2)t} & \frac{1-\cos\phi}{2} e^{-\gamma_1 t} \end{bmatrix}. \quad (\text{B7})$$

### Appendix C: QFI Calculation for the Steady-State Density Matrix

We start from the steady-state density matrix written in terms of its Bloch vector  $\mathbf{r} = (r_x, r_y, r_z)$ , with short-hands  $\zeta = r\tau g$ ,  $\gamma_1 = 1/T_1$ , and  $\gamma_2 = 1/T_2$ . For the noisy reservoir preparation used here one finds

$$r_x(\phi) = \frac{\zeta}{2} e^{-(\gamma_1+\gamma_2)t} \sin(2\phi), \quad (\text{C1})$$

$$r_y(\phi) = 0, \quad (\text{C2})$$

$$r_z(\phi) = e^{-\gamma_1 t} \cos\phi. \quad (\text{C3})$$

The Bloch vector components are defined as

$$r_x = \text{Tr}(\rho^{\text{ss}} \sigma_x), \quad r_y = \text{Tr}(\rho^{\text{ss}} \sigma_y), \quad r_z = \text{Tr}(\rho^{\text{ss}} \sigma_z),$$

where  $\rho^{\text{ss}}$  is the steady-state density matrix.

The  $\phi$ -derivatives of these components are

$$\partial_\phi r_x(\phi) = \zeta e^{-(\gamma_1+\gamma_2)t} \cos(2\phi), \quad (\text{C4})$$

$$\partial_\phi r_y(\phi) = 0, \quad (\text{C5})$$

$$\partial_\phi r_z(\phi) = -e^{-\gamma_1 t} \sin\phi. \quad (\text{C6})$$

From these, the squared norm of the derivative and the Bloch-vector inner product are

$$\begin{aligned} |\partial_\phi \mathbf{r}|^2 &= (\partial_\phi r_x)^2 + (\partial_\phi r_y)^2 + (\partial_\phi r_z)^2 \\ &= \zeta^2 e^{-2(\gamma_1+\gamma_2)t} \cos^2(2\phi) + e^{-2\gamma_1 t} \sin^2\phi, \end{aligned} \quad (\text{C7})$$

$$\begin{aligned} \mathbf{r} \cdot \partial_\phi \mathbf{r} &= r_x \partial_\phi r_x + r_y \partial_\phi r_y + r_z \partial_\phi r_z \\ &= \frac{1}{2} \sin(2\phi) \left[ \zeta^2 e^{-2(\gamma_1+\gamma_2)t} \cos(2\phi) - e^{-2\gamma_1 t} \right]. \end{aligned} \quad (\text{C8})$$

The Bloch-vector length is

$$\begin{aligned} |\mathbf{r}|^2 &= r_x^2 + r_y^2 + r_z^2 \\ &= \frac{\zeta^2}{4} e^{-2(\gamma_1+\gamma_2)t} \sin^2(2\phi) + e^{-2\gamma_1 t} \cos^2\phi. \end{aligned} \quad (\text{C9})$$

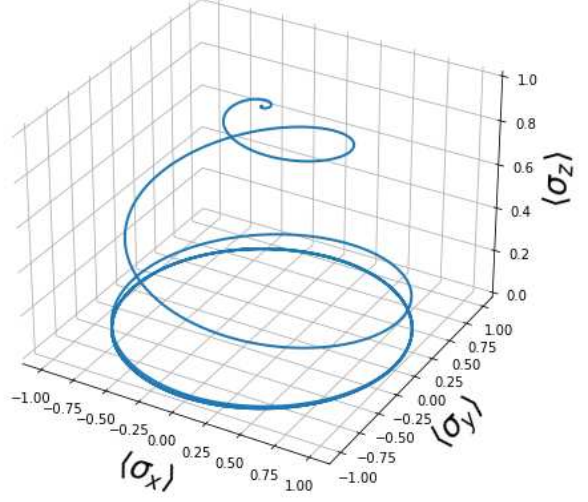


FIG. 5. Bloch–vector trajectory under a Gaussian–modulated  $x$ –drive that realizes  $R_x[\pi/2]$  within the open–system framework of Eqs. (9)–(10). Starting from the north pole ( $|0\rangle$  state), the vector follows a spiral path towards the equatorial plane, illustrating the combined effect of the coherent quarter–turn rotation and the dissipative processes characterized by  $T_1 = 150 \mu\text{s}$  and  $T_2 = 100 \mu\text{s}$ .

Finally, using the Bloch–form QFI for a single qubit,

$$\mathcal{F}_\phi = |\partial_\phi \mathbf{r}|^2 + \frac{(\mathbf{r} \cdot \partial_\phi \mathbf{r})^2}{1 - |\mathbf{r}|^2},$$

we obtain

$$\begin{aligned} \mathcal{F}_\phi &= \zeta^2 e^{-2(\gamma_1+\gamma_2)t} \cos^2(2\phi) + e^{-2\gamma_1 t} \sin^2\phi \\ &+ \frac{\frac{1}{4} \sin^2(2\phi) \left[ \zeta^2 e^{-2(\gamma_1+\gamma_2)t} \cos(2\phi) - e^{-2\gamma_1 t} \right]^2}{1 - e^{-2\gamma_1 t} \cos^2\phi - \frac{\zeta^2}{4} e^{-2(\gamma_1+\gamma_2)t} \sin^2(2\phi)}. \end{aligned} \quad (\text{C10})$$

This expression is algebraically equivalent to applying the two–level QFI formula in the main text to the steady-state density matrix, and it is well defined for mixed states with  $|\mathbf{r}| < 1$ .

### Appendix D: Algorithmic simulation

#### 1. The pulse amplitude

To define a dimensionless measure of the overall drive, we introduce  $\alpha$  as the time integral of the Rabi frequency:

$$\alpha = \int_{-\infty}^{\infty} \Omega(t) dt = \frac{\mu}{\hbar} \int_{-\infty}^{\infty} E(t) dt. \quad (\text{D1})$$

For a Gaussian drive field of the form

$$E(t) = A_0 \exp\left[-\frac{(t - t_c)^2}{\sigma_p^2}\right], \quad (\text{D2})$$

the integral evaluates to

$$\alpha = \frac{\mu A_0}{\hbar} \sqrt{\pi} \sigma_p. \quad (\text{D3})$$

Rearranging gives

$$A_0 = \frac{\alpha \hbar}{\mu \sqrt{\pi} \sigma_p}. \quad (\text{D4})$$

Since the Rabi frequency is  $\Omega(t) = \mu E(t)/\hbar$ , the peak value becomes

$$\Omega_0 = \frac{\mu A_0}{\hbar} = \frac{\alpha}{\sqrt{\pi} \sigma_p}. \quad (\text{D5})$$

This relation shows that the effective amplitude parameter  $\Omega_0$  used in the device-level description is determined solely by the normalized pulse area  $\alpha$  and the temporal width  $\sigma_p$ , independent of the dipole matrix element.

We simulate a single transmon operated as an effective two-level system (Figure 5) and driven along the  $x$  axis by a Gaussian-enveloped pulse within the open-system model of Eqs. (9)–(10). Throughout the numerics we set the qubit transition to  $\omega_0 = 2\pi \times 4.5$  GHz, which lies well inside the typical 4–6 GHz window for fixed-frequency

devices. The control envelope uses a temporal width  $\sigma_p = 22.4$  ns and a peak Rabi rate chosen via the pulse-area condition  $\alpha = \pi/2$ , so that the drive implements a quarter turn  $R_x[\pi/2]$  as in the hardware decomposition of  $H$ . All trajectories are obtained directly in the laboratory frame, since no rotating-frame transformation is applied.

## 2. Numerical evaluation of QFI

In practice the derivative  $\partial_\varphi \rho$  for Eq. (7) cannot be obtained analytically since  $\rho(\varphi)$  is generated by a full Lindblad time-evolution simulation. Instead, we approximate the derivative by a centered finite-difference formula,

$$\partial_\varphi \rho \approx \frac{\rho(\varphi + \delta\varphi) - \rho(\varphi - \delta\varphi)}{2 \delta\varphi}, \quad (\text{D6})$$

with  $\delta\varphi$  chosen sufficiently small to ensure convergence (here  $\delta\varphi \sim 10^{-4}$  was used). This approach is mathematically equivalent to a lowest-order finite element scheme, which balances numerical stability and computational cost. This procedure is repeated for each value of  $\varphi$  in the interval  $[0, 2\pi]$ . In practice, a discretization grid of  $N=50$  phase points is sufficient to resolve the oscillatory structure of  $\mathcal{F}_\varphi$ . Each point requires three independent device-level simulations, so that the final curve reflects approximately  $3N$  full Lindblad evolutions.

---

[1] J. Preskill, *Quantum* **2**, 79 (2018).

[2] P. W. Shor, *Physical Review A* **52**, R2493 (1995).

[3] E. Knill and R. Laflamme, *Physical Review A* **55**, 900 (1997).

[4] A. G. Fowler, M. Mariantoni, J. M. Martinis, and A. N. Cleland, *Physical Review A* **86**, 032324 (2012).

[5] R. Barends, J. Kelly, A. Megrant, A. Veitia, D. Sank, E. Jeffrey, T. C. White, J. Mutus, A. G. Fowler, B. Campbell, Y. Chen, Z. Chen, B. Chiaro, A. Dunsworth, C. Neill, P. O’Malley, P. Roushan, A. Vainsencher, J. Wenner, A. N. Korotkov, A. N. Cleland, and J. M. Martinis, *NATURE* **508**, 10.1038/nature13171 (2014).

[6] C. Ryan-Anderson, J. Bohnet, K. Lee, D. Gresh, A. Hankin, J. Gaebler, D. Francois, A. Chernoguzov, D. Lucchetti, N. Brown, T. Gatterman, S. Halit, K. Gilmore, J. Gerber, B. Neyenhuis, D. Hayes, and R. Stutz, *Physical Review X* **11**, 041058 (2021).

[7] R. Acharya, others, and Google Quantum AI and Collaborators, *Nature* **638**, 920 (2025).

[8] P. W. Shor, in *Proceedings 35th Annual Symposium on Foundations of Computer Science* (IEEE, 1994) pp. 124–134.

[9] A. W. Harrow, A. Hassidim, and S. Lloyd, *Physical Review Letters* **103**, 150502 (2009).

[10] W. H. Zurek, *Reviews of Modern Physics* **75**, 715 (2003).

[11] D. C. McKay, S. Sheldon, J. A. Smolin, J. M. Chow, and J. M. Gambetta, *Physical Review Letters* **122**, 200502 (2019).

[12] Y. L. Len, T. Gefen, A. Retzker, and J. Kołodyński, *Nature Communications* **13**, 6971 (2022).

[13] S. Zhou, S. Michalakis, and T. Gefen, *PRX Quantum* **4**, 040305 (2023).

[14] D. Šafránek, *Physical Review A* **97**, 042322 (2018).

[15] J. Liu, H. Yuan, X.-M. Lu, and X. Wang, *Journal of Physics A: Mathematical and Theoretical* **53**, 023001 (2020).

[16] V. Scarani, M. Ziman, P. Štelmachovič, N. Gisin, and V. Bužek, *Physical Review Letters* **88**, 097905 (2002).

[17] M. Ziman, P. Štelmachovič, V. Bužek, M. Hillery, V. Scarani, and N. Gisin, *Physical Review A* **65**, 042105 (2002).

[18] D. Nagaj, P. Štelmachovič, V. Bužek, and M. Kim, *Physical Review A* **66**, 062307 (2002).

[19] M. Cattaneo, G. De Chiara, S. Maniscalco, R. Zambrini, and G. L. Giorgi, *Physical Review Letters* **126**, 130403 (2021).

[20] D. Karevski and T. Platini, *Physical Review Letters* **102**, 207207 (2009).

[21] S. of Computer Science, and V. Scarani, *Physical Review E* **99**, 042103 (2019).

[22] F. Ciccarello, S. Lorenzo, V. Giovannetti, and G. M. Palma, *Physics Reports Quantum collision models: Open system dynamics* (2024).

[23] G. O. Alves, M. A. F. Santos, and G. T. Landi, *Physical Review A* **110**, 052421 (2024).

[24] S. Deffner and C. Jarzynski, *Physical Review X* **3**, 041003 (2013).

[25] S. Deffner, *Physical Review E* **88**, 062128 (2013).

[26] U. Korkmaz and D. Türkpençe, *Physics Letters A* **426**, 127887 (2022).

[27] U. Korkmaz and D. Türkpençe, *Physical Review A* **107**, 012432 (2023).

[28] L. Pezzé and A. Smerzi, *Physical Review Letters* **100**, 073601 (2008).

[29] J. P. Dowling, *Contemporary Physics* **49**, 125 (2008).

[30] V. Giovannetti, S. Lloyd, and L. Maccone, *Nature Photonics* **5**, 222 (2011).

[31] L. Pezzé, A. Smerzi, M. K. Oberthaler, R. Schmied, and P. Treutlein, *Reviews of Modern Physics* **90**, 035005 (2018).

[32] D. Türkpençe and R. Román-Ancheyta, *JOSA B* **36**, 1252 (2019).

[33] R. Román-Ancheyta, B. Çakmak, and Ö. E. Müstecaplıoğlu, *Quantum Science and Technology* **5**, 015003 (2019).

[34] C. W. Helstrom, *Journal of Statistical Physics* **1**, 231 (1969).

[35] S. L. Braunstein and C. M. Caves, *Physical Review Letters* **72**, 3439 (1994), publisher: American Physical Society.

[36] J. Dittmann, *Journal of Physics A: Mathematical and General* **37**, 103201 (2004).

[37] W. Zhong, Z. Sun, J. Ma, X. Wang, and F. Nori, *Physical Review A* **87**, 022337 (2013).

[38] H.-P. Breuer and F. Petruccione, *The Theory of Open Quantum Systems* (Oxford University Press, Oxford, 2010).

[39] F. Motzoi, J. M. Gambetta, P. Rebentrost, and F. K. Wilhelm, *Physical Review Letters* **103**, 110501 (2009).

[40] J. M. Chow, L. DiCarlo, J. M. Gambetta, F. Motzoi, L. Frunzio, S. M. Girvin, and R. J. Schoelkopf, *Physical Review A* **82**, 040305 (2010).

[41] F. Verstraete, M. M. Wolf, and J. Ignacio Cirac, *Nature Physics* **5**, 633 (2009).

[42] R. Blume-Kohout and W. H. Zurek, *Foundations of Physics* **35**, 1857 (2005).

[43] M. Zwolak and W. H. Zurek, *Physical Review A* **95**, 030101 (2017).

[44] J. R. Johansson, P. D. Nation, and F. Nori, *Computer Physics Communications* **184**, 1234 (2013).

[45] IBM Quantum experience, <https://quantum-computing.ibm.com/> (2025), accessed: 2025-08-07.

[46] P. Filipowicz, J. Javanainen, and P. Meystre, *Physical Review A* **34**, 3077 (1986).

[47] J. D. Cresser, *Physical Review A* **46**, 5913 (1992).

[48] J.-Q. Liao, H. Dong, and C. P. Sun, *Physical Review A* **81**, 052121 (2010).

[49] D. Türkpençe and Ö. E. Müstecaplıoğlu, *Physical Review E* **93**, 012145 (2016).

[50] K. Ullah, E. Köse, R. Yagan, M. C. Onbaşlı, and Ö. E. Müstecaplıoğlu, *Phys. Rev. Research* **4**, 023221 (2022).

[51] R. Huang, Q.-Y. Cai, F. Nosrati, R. Lo Franco, and Z.-X. Man, *Quantum Science and Technology* **10**, 035001 (2025).

[52] T. Alexander, N. Kanazawa, D. J. Egger, L. Capelluto, C. J. Wood, A. Javadi-Abhari, and D. C McKay, *Quantum Science and Technology* **5**, 044006 (2020).

[53] B. Li, S. Ahmed, S. Saraogi, N. Lambert, F. Nori, A. Pitchford, and N. Shammah, *Quantum* **6**, 630 (2022).

[54] E. Hyypä, A. Vepsäläinen, M. Papić, C. F. Chan, S. Inel, A. Landra, W. Liu, J. Luus, F. Marxer, S. Ockeloen-Korppi, S. Orbell, B. Tarasinski, and J. Heinsoo, *PRX Quantum* **5**, 030353 (2024).

[55] J. Roffe, *Contemporary Physics* **60**, 226 (2019).

[56] Y. Akahoshi, *PRX Quantum* **5**, 10.1103/PRXQuantum.5.010337 (2024).

[57] S. Huang, *Physical Review Letters* **127**, 10.1103/PhysRevLett.127.090505 (2021).

[58] J. P. Bonilla Ataides, D. K. Tuckett, S. D. Bartlett, S. T. Flammia, and B. J. Brown, *Nature Communications* **12**, 2172 (2021).

[59] S. Sivarajah, S. Dilkes, A. Cowtan, W. Simmons, A. Edgington, and R. Duncan, *Quantum Science and Technology* **6**, 014003 (2020).

[60] F. Motzoi and F. K. Wilhelm, *Physical Review A* **88**, 10.1103/PhysRevA.88.062318 (2013).